Available online at www.sciencedirect.com

jmr&t
Journal of Materials Research and Technology

journal homepage: www.elsevier.com/locate/jmrt

Quantification of damage evolution in stainless steel 316L based on 3D *ex-situ* X-ray CT and micro-damage model

Xianzheng Lu [a,b,*], *Chiping Lai* [b], *Luenchow Chan* [b]

[a] *Hunan Provincial Key Laboratory of Intelligent Manufacturing Technology for High-performance Mechanical Equipment, Changsha University of Science and Technology, Changsha, 410114, China*
[b] *Department of Industrial and Systems Engineering, Research Institute for Advanced Manufacturing, The Hong Kong Polytechnic University, Hung Hom, Kowloon, S.A.R., Hong Kong*

ARTICLE INFO

Article history:
Received 7 April 2023
Accepted 15 June 2023
Available online 19 June 2023

Keywords:
Damage evolution
Stainless steel 316L
X-ray computed tomography
Micro-voids
Micromechanics-based damage model

ABSTRACT

Quantifying damage to improve the constitutive models that better account for damage prediction is of great importance in metal forming process. In this study, high-resolution micro-focus X-ray Computed tomography (CT) system, together with loading-unloading tensile test, were employed to quantify the 3D interactions of micro-voids evolution in the biocompatible alloy stainless steel 316L (SS316L). The specimen material was tensile deformed and interrupted at several strain intervals prior to failure, X-ray CT was then performed to quantify the damage evolution via the detected changing in size, number, distribution, and volume fraction of micro-voids (VFMV) after each specified strain increment. Thereby the nature of ductile damage, which involved the dynamic evolution mechanism of the nucleation, growth and coalescence of micro-voids, was revealed. Furthermore, an improved micromechanics-based damage (micro-damage) model considering large deformation condition was implemented into finite element (FE) package ABAQUS for the damage prediction. The damage of the specimen under tensile deformation with a wide range of stress states was predicted and a good agreement with experimental data was achieved in terms of damage distribution and evolution. It is concluded that the findings of this study not only reveal the dynamic evolution mechanism of the micro-voids in the damage process intuitively from the experimental point of view, but also provide more accurate material parameters for the theoretical damage modelling, so as to obtain more convincible damage prediction results in the metal forming process.

1. Introduction

Ductile damage is most common in metallic materials under plastic deformation conditions [1], which is basically caused by the nucleation, growth and coalescence of micro-defects such as micro-cracks/voids, impurities and inclusions, etc. Therefore, the identification and quantification of damage in terms of experimental method and theoretical modelling is of great importance in metal forming process. For the

* Corresponding author. Hunan Provincial Key Laboratory of Intelligent Manufacturing Technology for High-performance Mechanical Equipment, Changsha University of Science and Technology, Changsha, 410114, China.
E-mail address: xzlucsu@163.com (X. Lu).
https://doi.org/10.1016/j.jmrt.2023.06.160

experimental aspect, destructive methods are used commonly for the defect analysis, and the defect volume fraction is always evaluated by quantitative metallographic analysis or microscopic examinations [2]. However, not only were the traditional destructive testing methods laborious and tedious, but also the material was destroyed completely and unusable. For the materials or components with high safety considerations, e.g., those used in medical implantations, aviation and automotive industry, a fatal defect may result in serious consequences.

Thus, non-destructive testing (NDT) becomes a highly valuable technology that can evaluate the quality of the product effectively and efficiently. X-ray Computed tomography (CT) is a kind of NDT technology that reconstructs internal structure images of objects based on external projection data [3]. It is an analysis technique for the three-dimensional (3D) visualization of a test part regarding its geometry and density. By collecting several X-ray images at a defined trajectory, a 3D-model of the part can be reconstructed. X-ray CT involves a wide range of promising detection tools to evaluate the properties of a material, component or system without causing damage [4]. In addition, the combination of X-ray CT scanning and volumetric digital image correlation (DIC) provides a deep understanding of the damage/fracture mechanisms in the process of material deformation [5,6]. Therefore, the application of X-ray CT technology for all-round micro-defect detection and further for damage identification has attracted much interest in recent years, and researchers have found that the intrinsic nature (i.e.: grain size, texture, micro-defects, etc.) had significant influences on the crack initiation/location and propagation, damage evolution, fatigue and final fracture for different types of materials (e.g.: metals, polymers, composites, etc.) under different loading conditions such as tension, compression and fatigue loading [7–13].

As for the theoretical modelling of damage evolution, owing to the well-developed solid mechanics theories and the rapid progress of computational technologies, numerical simulations with analytical finite element (FE) models allow for the efficient evaluation of various material forming issues, and the microstructure evolution, phase transformation and damage propagation under tension/compression can be well predicted by finite element modelling [14–16]. There are two main computational approaches used for damage prediction in metallic materials, i.e., the phenomenological continuum damage mechanics (CDM)-based model and the micromechanics-based damage (micro-damage) model. The former of these uses continuum thermodynamics and continuum mechanics to study the effects of damage on the mechanical response induced by irreversible processes [17]. It focuses on the effects of damage on the macroscopic mechanical properties, as well as the processes and laws of damage evolution of materials and structures, without examining the microscopic physical and mechanical processes [18]. The tenet of the CDM approach is that the predicted macroscopic mechanical and deformation behavior are in accordance with the experimental results and the actual situation. The second approach, i.e., the micro-damage model, adopts a constitutive model to evaluate the effects of various primitives, such as micro-cracks, micro-voids, shear bands, etc., inside the material. It was originally developed by Gurson and further known as GTN model [19,20]. In the GTN model, ductile fracture occurs through void nucleation, growth, and coalescence. The void coalescence can be triggered by localized plastic deformation within the gap of inter-void ligament between adjacent voids and can be modelled by accelerating void growth at a critical void volume fraction.

Due to the sound physical understanding of damage caused fundamentally by micro-void evolution in metallic material, the micro-damage model is used widely nowadays in various metal forming processes (e.g., sheet metal forming, rolling, extrusion, forging, additive manufacturing, etc.) under different loading conditions (e.g., complex stress triaxialities, shear loading, large strain, high strain rate states, etc.) [21–25]. Attention was also paid to the combination of the X-ray CT techniques and micro-damage model for better prediction of ductile damage in different metallic materials. Williams et al. analyzed the void growth and particle fracture in SiC particle reinforced Al alloy composites using X-ray CT, and the micro-mechanisms of fracture and the quantitative effects of particle size and aspect ratio were obtained [26]. Cao et al. studied the ductile damage mechanisms for a high carbon steel by *in-situ* X-ray micro-tomography tensile test, and then an improved GTN model which considered the shear loading condition was established. The predicted results showed good agreement with the experiments under different loading configurations [27]. Kaye et al. conducted *ex-situ* synchrotron X-ray CT scanning to quantify the initiation and growth of inclusion for free cutting steel during hot deformation at different interrupt strains, a new parameter for modelling 3D damage evolution was proposed and the damage localization was confirmed with a 3D micromechanics model [28]. Roth et al. provided the tomographic evidence that ductile damage was caused by the evolution of micro-voids under shear-dominated loading, and the ductile fracture of a representative volume element was further predicted by a micromechanical based damage model [4]. Lu and Chan analyzed the 3D micro-void distribution and evolution inside the biocompatible alloys stainless steel 316L and Ti alloy Ti–6Al–4V through X-ray CT quantitatively. And the localized damage evolutions were well predicted by an improved thermo-mechanical coupled micro-damage model [29]. By combining the interrupted tensile testing and X-ray tomography, the internal damage evolution in two types of steel was identified by Suárez et al. [30]. In addition, the predicted material behaviors can be reproduced well by using a Gurson model. Xing et al. developed a micro-damage model which considered the mutual effects between microstructure, micro-macro deformation, and damage for aluminum alloys under tension-dominated loading conditions [31]. In which, the model parameters were determined via *in-situ* X-ray CT and load–displacement curves. Simulation results indicated that the model was capable to predict the deformation response and damage behavior of multiphase metals.

Although much of the research related to the ductile damage prediction has been done on different metal materials under various forming processes, the existence of accurate micro-void modelling and its subsequent evolution for damage prediction within the micro-damage model framework is not so thorough. Therefore, the primary objective of this study was to experimentally reveal the nature of ductile damage

during metal forming and then to adopt an improved micro-damage model for damage prediction. Biocompatible alloy stainless steel 316L (SS316L) was selected as the specimen material, high-resolution micro-focus X-ray CT system and loading-unloading tensile test were employed to quantify the 3D interactions of micro-voids evolution. An improved micro-damage model was then implemented into FE package ABAQUS for damage prediction. The damage under tensile deformation with a wide range of stress states was predicted and further compared with experimental data for verification.

2. Experimental details

2.1. Material and specimen preparation

The material used in this study was cast SS316L with chemical composition shown in Table 1. Several types of specimens were designed and fabricated for mechanical testing and X-ray CT scanning. Specimens used for uniaxial compression tests to obtain the elastic–plastic material properties were designed according to the ASTM standard E9-09, i.e., a cylinder with size of Ø8 mm × 12 mm. Specimens employed for both X-ray CT scanning and loading-unloading tensile test were designed to be small-scaled and proportional to standard one (ASTM standard E8M–09), thus to better detect the evolution of tiny internal micro-voids and ensure the full penetration of X-ray source. In addition, to obtain a wide range of stress states and consider the stress triaxiality effects [32,33], round bar (RB) tensile specimens and notched round bar (NRB) tensile specimens with notch radius of 2 mm and 10 mm (hereinafter represented as NRB2 and NRB10 respectively) were designed, as shown in Fig. 1.

2.2. X-ray CT scanning

A non-destructive high-resolution micro-focus X-ray CT system YXLON FF35 CT was employed to investigate the initiation and evolution of micro-voids inside the specimen in the initial and then after each designated deformation stage. Because the two ends of the tensile specimen were clamped by the alignment fixtures, only the middle part of gauge length of the specimen, with an approximate size of Ø4.0 mm × 5.0 mm (region of interest, ROI), was scanned by the X-ray.

The installed high-resolution transmission tube enabled the system to detect the small-sized voids up to 0.5 μm in the material. To ensure the full penetration of the X-ray source on the specimen material for obtaining high-quality CT images with good contrast, it was of great importance to select appropriate tube voltages and currents as well as other scan parameters. In addition, parameters such as magnification, number of projections, frame rate are also key settings that determine the scanning quality. Table 2 summarizes the parameters setting for the X-ray CT scanning in this study.

Two-dimensional (2D) projections were obtained by rotating the specimen through 360°. Then, the 3D volumetric CT data were generated using the in-house CERA reconstruction spooler. 2D and 3D CT images were visualized with VGStudio MAX 2.2 (Volume Graphics GmbH, Germany). An advanced segmentation algorithm was used for defect detection inside the specimen, which allowed for the variation in grey values, including noise reduction at the locations of seed points and the identification of defects connected to the surrounding air. The defect detection contained the information about the probability that it was a real defect. Based on the detection results, the threshold values could be specified so that only defects with the probabilities above the threshold were contained in the detection results. Hence, information like size, number, spatial location, compactness, and sphericity of micro-voids could be obtained. These data were further analyzed for the damage evolution identification, details refer to Section 4.2.

Table 1 – Chemical composition (% in mass) of cast SS316 L used in this study.

C	Mn	S	Si	Cr	Ni	Mo	Fe
0.024	1.68	0.003	0.03	16.73	11.55	1.52	balance

2.3. Uniaxial compression test and loading-unloading tensile test

In this study, both uniaxial compression test and loading-unloading tensile test were conducted on an MTS 810 testing machine with a load capacity of 100 kN. The former is performed to acquire the elastic and plastic deformation related material parameters for damage prediction, while the latter is employed for detecting micro-void evolution at different deformation stages. Since tensile testing would inevitably lead to yield and fracture, while compression test can reflect the plastic hardening stage of the material stably, and our previous study has shown that similar stress–strain data of the elastic and plastic hardening parts was obtained from both tensile and compression tests [34], compression test rather than tensile test was chosen for the parameter acquisition related to elastic and plastic deformations. For uniaxial compression test, colloidal graphite was smeared on the surface of each specimen to minimize the barreling effects during the compression. The strain was measured using extensometer with a gauge length of 10 mm and controlled at the rates of 0.001 s^{-1}, 0.01 s^{-1} and 0.1 s^{-1}, the uniaxial compressive loading was gradually increased until a deformation of 30% was reached. For loading-unloading tensile test, the tensile force was applied on the specimen and increased gradually until a default pause strain value was reached. Then the specimen was unloaded to an almost loading-free state. Afterward, it was unmounted from the MTS 810 machine and prepared for the subsequent X-ray CT scanning. Once the X-ray CT testing finished, the specimen was mounted again on the MTS 810 machine; this test procedure was repeated until the specimen fractured. At each loading-unloading test cycle, the pause strain values were set as 4% and the axial strain was measured by an extensometer with gauge length of 10 mm. The loading stages were strain-controlled at a rate of 0.001 s^{-1}, while the unloading stages were set as force-controlled at a rate of −0.5 kN/s. In addition, uniaxial tensile test for the RB, NRB10 and NRB2 specimens with strain rate of 0.001 s^{-1} up to fracture was performed, and the obtained experimental load-

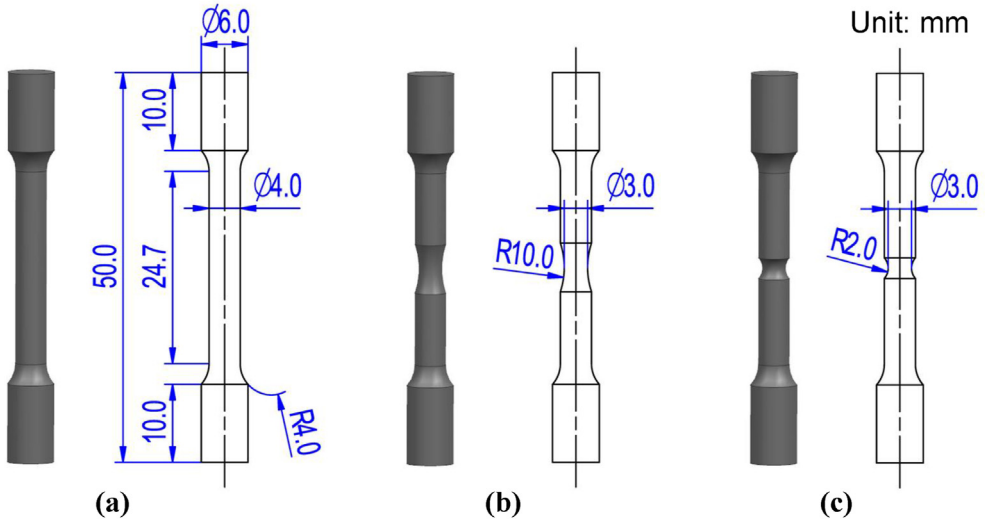

Fig. 1 – Specimens designed for X-ray CT scanning and loading-unloading tensile test: (a) RB, (b) NRB10 and (c) NRB2.

elongation curves will be compared with the predicted results for the verification [35].

3. Micro-damage model for damage evolution prediction

3.1. *Constitutive equations and FE implementation*

In this study, a micromechanics-based damage (micro-damage) model considering large deformation was developed. Based on hypo-elastic relations, the specific constitutive equations of the micro-damage model were deduced [36]. First, the Hencky's logarithmic strain h is decomposed into two parts, h^e and h^p, to describe the elastic–plastic behavior of metallic materials respectively [37]. For large deformations, the h can be replaced by stretching tensor D and formulated as [38].

$$\mathbf{D} = \mathbf{D}^e + \mathbf{D}^p \tag{1}$$

where superscript e and p indicate the elastic and plastic parts, respectively. Further, the elastic strain tensor $\mathbf{h}^e$ can be regarded as a state variable to formulate the constitutive equations, and the elastic stretching tensors $\mathbf{D}^e$ can be formulated according to the hypo-elastic relationship as

$$\mathbf{D}^e = \frac{1+\nu}{E}\mathring{\boldsymbol{\tau}}^{\log} - \frac{\nu}{E}\mathrm{tr}(\dot{\boldsymbol{\tau}})\mathbf{1} \tag{2}$$

where τ, E and ν are Kirchhoff stress tensor, Young's modulus and Poisson's ratio, respectively.

In addition, the plastic stretching tensors $\mathbf{D}^p$ can be decomposed into the deviatoric stress tensor $\mathbf{D}^{p'}$ and the hydrostatic stress tensor $\mathbf{D}^{p(m)}$ and given as

$$\mathbf{D}^p = \mathbf{D}^{p'} + \mathbf{D}^{p(m)} = \mathbf{D}^{p'} + \frac{1}{3}\mathrm{tr}(\mathbf{D}^p)\mathbf{1} \tag{3}$$

In this study, the damage variable f, i.e., volume fraction of micro-voids (VFMVs), was introduced, hence the flow rules $\mathbf{D}^{p'}$ and $\mathbf{D}^{p(m)}$ can be defined as

$$\mathbf{D}^{p'} = \sqrt{\frac{3}{2}}\dot{p}\mathbf{N} = \sqrt{\frac{3}{2}}\left(\frac{F_y}{K}\right)^n\mathbf{N} \tag{4}$$

$$\mathbf{D}^{p(m)} = \frac{1}{3}fs_1\exp\left(\frac{\mathrm{tr}(\boldsymbol{\tau})}{3s_2\rho}\right)\dot{p}\mathbf{1} \tag{5}$$

where $\dot{p}$ is the accumulated plastic strain rate, n and K are the material viscosity constants. s_1 and s_2 are damage parameters, $\langle\rangle$ is the McCauley operator; $\mathbf{N} = \frac{\boldsymbol{\tau}'}{\|\boldsymbol{\tau}'\|}$ is the unit normal vector of the yield surface F_y.

Furthermore, the yield surface of F_y can be expressed as [39].

$$F_y = \sqrt{\frac{3}{2}}\|\boldsymbol{\tau}'/\rho\| + fs_1s_2\exp\left(\frac{\mathrm{tr}(\boldsymbol{\tau})}{3s_2\rho}\right) - Q \tag{6}$$

In this study, the isotropic hardening rule was adopted, thus the deformation resistance Q consists of two parts as

Table 2 – The parameters setting for X-ray CT scanning in this study.

Tube voltage (kV)	Tube current (μA)	Magnification	No. Of 2D projections	Frame rate (Hz)	Frames per projection
115	105	16	1080	3.0	4

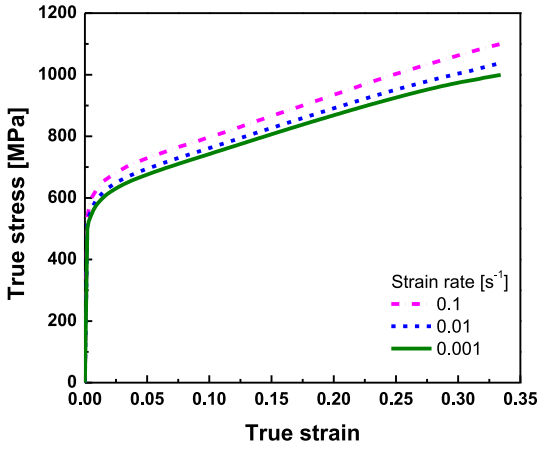

Fig. 2 – The experimental compressive stress–strain curves of the cast SS316 L specimen.

Table 3 – Material parameters of the cast SS316 L used for micro-damage model.

E (GPa)	υ	Q_0 (MPa)	R^{sat} (MPa)	β	K	n	s_1	s_2
190	0.3	472	590	3.0	230	8.2	2	173

$$Q = Q_0 + R \tag{7}$$

where Q_0 is the initial deformation resistance and R is the subsequent resistance.

The evolution law of R can be formulated as

$$\dot{R} = \beta(R^{sat} - R)\dot{p} \tag{8}$$

where R^{sat} denotes the saturated value of R and β is the evolution rate of R.

According to the mass conservation and the effective stress concept [40], the damage evolution law of f can be given as

$$\dot{f} = \rho \mathrm{tr}(\mathbf{D}^p) = \rho f s_1 \exp\left(\frac{\mathrm{tr}(\tau)}{3 s_2 \rho}\right)\dot{p} \tag{9}$$

The driving force is expressed as

$$F_f = \frac{s_2}{\rho_0}\ln\left(\frac{f(1-f_0)}{f_0(1-f)}\right) \tag{10}$$

where ρ_0 and f_0 are the initial density and initial VFMVs for a given material.

The above proposed micro-damage model was then implemented into the FE package ABAQUS using the subroutine UMAT. Details about the discretization of constitutive equations and implicit stress integration algorithm can refer to our published work [34].

3.2. *FE models and parameters identification for damage prediction*

Different geometrical models of SS316L specimens were designed for damage prediction with a wide range of stress states. Round bar (RB) and notched round bar (NRB) tensile specimens with the same size of that experimental ones were performed for damage prediction in tensile deformation, as shown in previous Fig. 1.

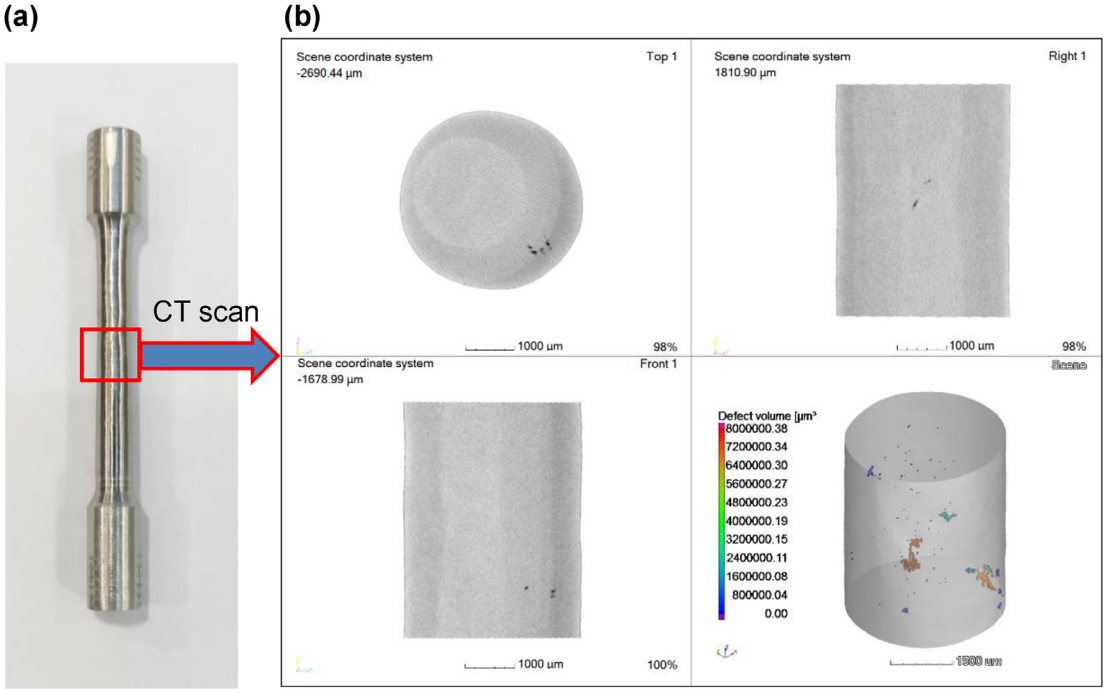

Fig. 3 – (a) RB tensile specimen of SS316 L and (b) middle part of gauge length (approx. Ø4.0 mm × 5.0 mm) for CT scanning and its 2D and 3D CT images with micro-voids.

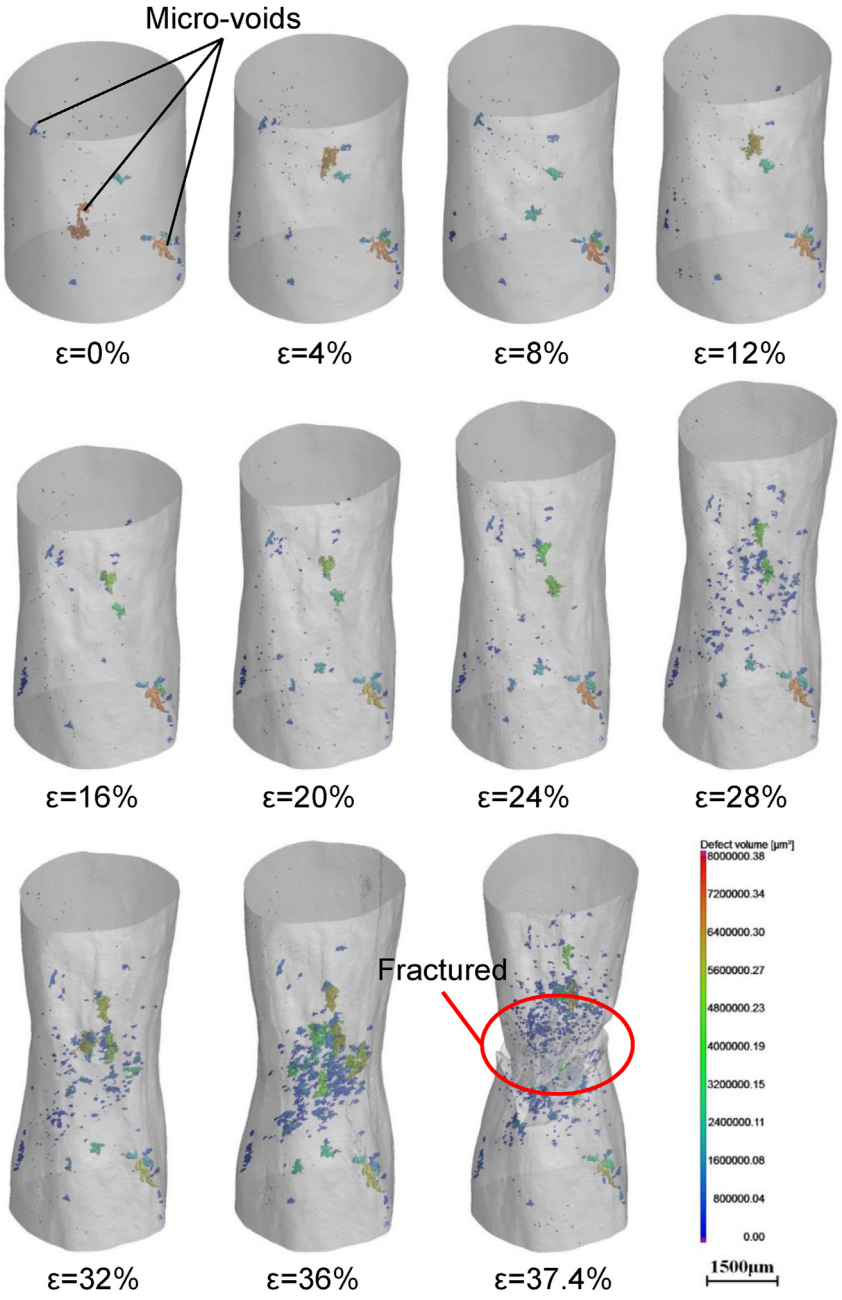

Fig. 4 – Micro-void evolution at different tensile strains of the RB tensile specimen.

For the FE simulations, the above-mentioned geometrical models were simplified as 2D axisymmetric and meshed with 2D 4-node bilinear axisymmetric quadrilateral elements (CAX4). Auto-remeshing functions were used to solve the stress concentration during the simulation. Boundary conditions are set at both ends of the tensile specimen, i.e., fixed constraint is applied on the nodes of the bottom line and the axial displacement is imposed on the nodes of the top line with a constant strain rate of 0.001 s^{-1}. The micro-damage model proposed in Section 3.1, including the evolution laws of visco-plastic flow rules (Eqs. (4) and (5)), yield function (Eq. (6)), isotropic hardening rule (Eq. (8)) and damage evolution law (Eq. (9)), was compiled and implemented into ABAQUS using a user defined material subroutine UMAT. The material parameters, such as Young's modulus, visco-plastic constants (K and n) and yield stress (Q_0 and R^{sat}) involved in the constitutive equations can be obtained through fitting the experimental compressive stress–strain curves. The initial damage value f_0 of each specimen can be determined by the X-ray CT scanning, i.e., the total volume of the micro-voids in the ROI divided by the volume of the ROI. For the damage parameters s_1 and s_2, s_1 is considered as a material-independent and the value of 2 is commonly adopted for most metallic materials [41], s_2 can be calibrated by the hardening part of stress–strain

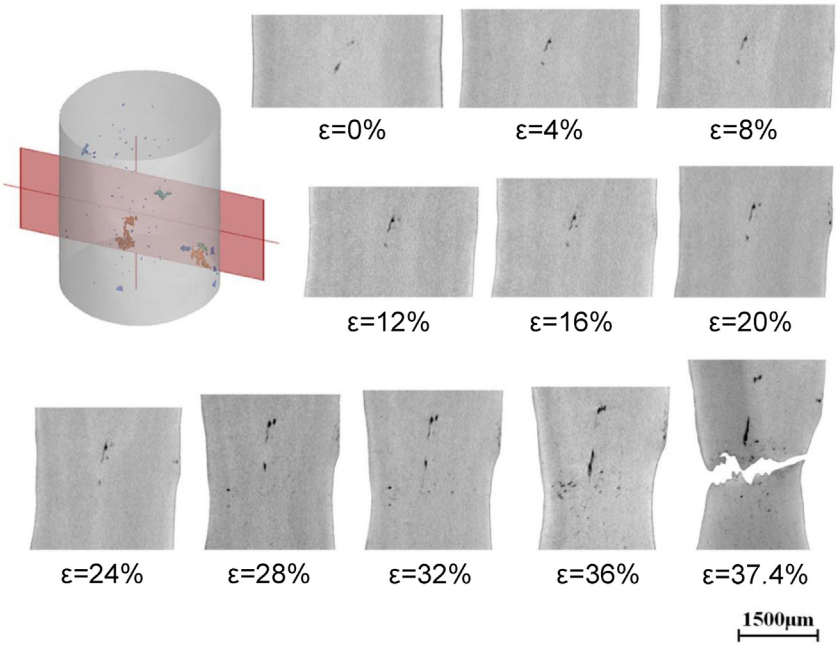

Fig. 5 – The specified cross-section of the gauge part and its micro-void evolution at different tensile strains.

curve. Details about the identification of material parameters can be found in our published work [34].

4. Results and discussions

4.1. *Experimental stress–strain curves*

The compressive stress–strain curves of the cast SS316L at strain rates of 0.001 s^{-1}, 0.01 s^{-1} and 0.1 s^{-1} are shown in Fig. 2. For the elastic deformation stage, a rate-independent elastic modulus with value of 190 GPa is measured. For the plastic deformation stage, remarkable rate-dependence and strain-hardening effect were observed. Specifically, the yield stress increased with the increasing of strain rate, and the strain-hardening made the stress increased linearly after yielding. Furthermore, the material parameters required in the micro-damage model can be obtained according to the method described in Section 3.2, and the determined parameters are illustrated in Table 3.

4.2. *Quantitative analysis of damage initiation and evolution*

4.2.1. *Round bar (RB) tensile specimen*

In this study, the X-ray CT system YXLON FF35 CT was employed to trace and measure the micro-voids inside the specimen directly. In this process, the micro-voids inside the

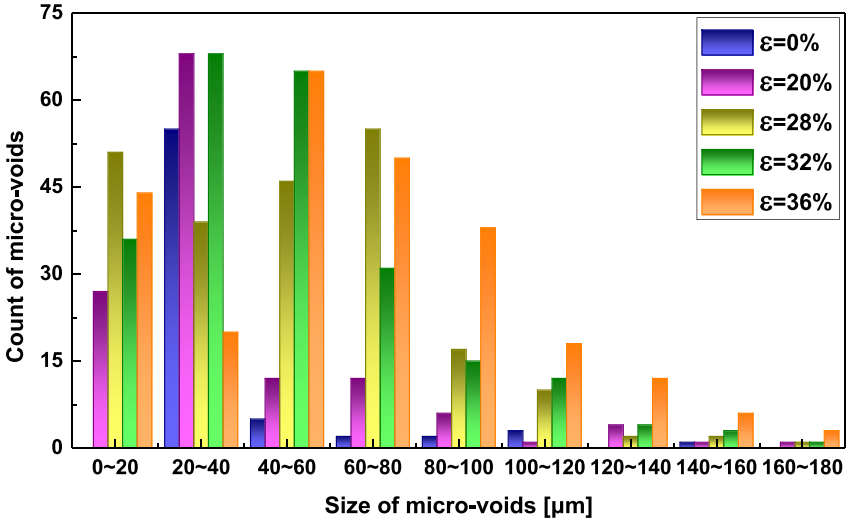

Fig. 6 – Sizes distribution of micro-voids for RB specimen at different strain levels.

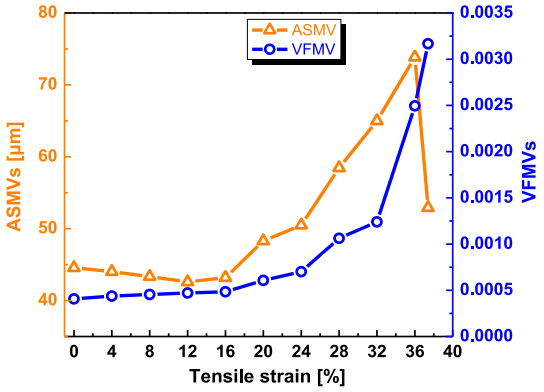

Fig. 7 – ASMVs and VFMVs of the RB specimen during tensile deformation.

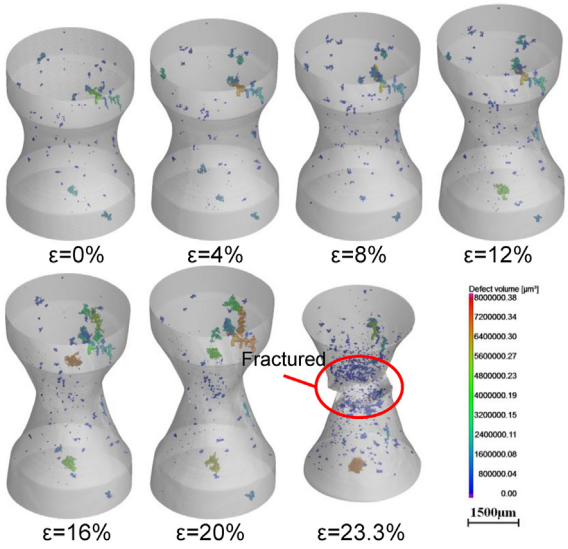

Fig. 9 – Micro-void evolution at different tensile strains of the NRB specimen (NRB2).

material could be modelled precisely and accurately. Fig. 3a shows the RB tensile specimen used for CT scanning and loading-unloading tensile test, in which the middle part of gauge length with an approximate size of Ø4.0 mm × 5.0 mm was CT scanned. Both the 2D and 3D CT images of the virgin (un-deformed) part with a 13.5 μm resolution were reconstructed and visualized, as shown in Fig. 3b.

The micro-voids inside the specimen material were analyzed quantitatively using the defect detection mode in VGStudio MAX 2.2. To better visualize the internal micro-voids of the material, the 3D CT images of the scanned specimen were displayed semi-transparently, as shown in the lower right of Fig. 3b. The material is represented in grey and the micro-voids with different volumes are represented in other colors. It was found that the micro-void distribution was not uniform throughout the specimen, the shapes of the micro-voids varied a lot, and the sizes of micro-voids ranged from 25.2 μm to 157.3 μm, indicating that the casting process left micro-voids randomly.

Furthermore, the identification of damage evolution from micro-voids was achieved by *ex-situ* X-ray CT scanning, i.e., loading-unloading tensile testing followed by X-ray CT scanning. By selecting specific feature elements, such as fillets, fixed planes, etc., it is possible to locate the same position at each scanning, thus the change of a particular micro-void can be roughly identified and tracked. Since the specimen was finally fractured at a tensile strain of 37.4%, the micro-void

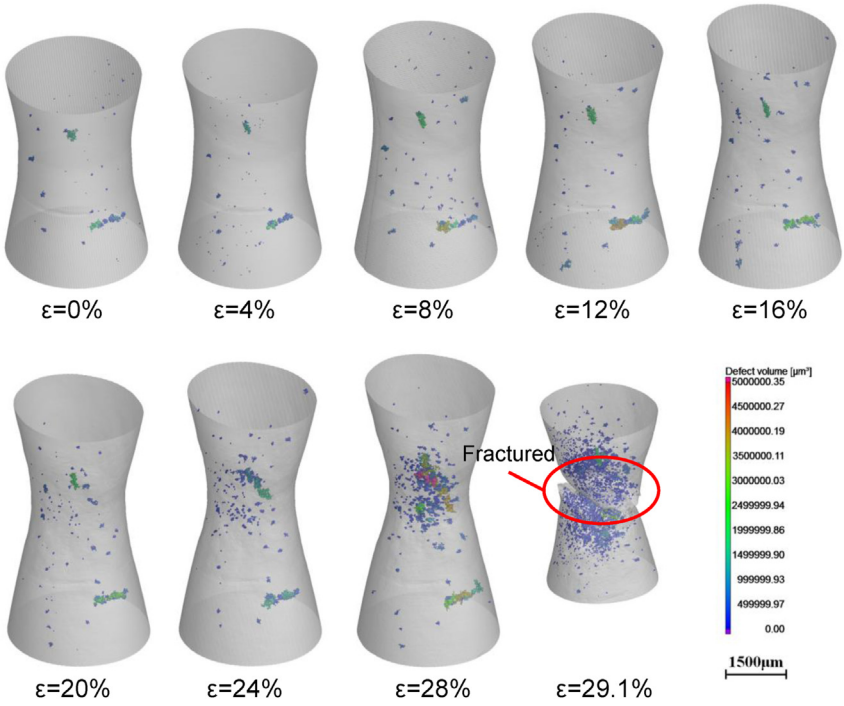

Fig. 8 – Micro-void evolution at different tensile strains of the NRB specimen (NRB10).

evolutions at strains of 0%, 4%, 8%, 12%, 16%, 20%, 24%, 28%, 32%, 36% and 37.4% were obtained, as shown in Fig. 4. For a better investigation of the micro-void evolution, a specified cross-section inside the gauge part as well as its micro-void evolution at different tensile strains are shown in Fig. 5. By combining Figs. 4 and 5, it can be seen that there were no obvious changes in micro-voids until the strain reached 20%. After that, the sizes of those inherent micro-voids in the middle of the specimen began to increase, and, meanwhile, some new small-sized (i.e., ranged 0–20 μm) micro-voids initiated. When the tensile strain increased further to 28%, the inherent micro-voids increased significantly and a large number of micro-voids initiated, resulting in the occurrence of necking at the corresponding region. With the further aggravation of the necking, the growth and coalescence of micro-voids became more and more obvious. Finally, the rapid increases in the size and number of micro-voids, as well as the coalescence of adjacent micro-voids, weakened the loading capability of the material, thus leading to complete failure of the specimen at a strain of 37.4%.

The quantitative analysis of the size distribution of micro-voids at different strain levels is shown in Fig. 6. Since the sizes and numbers of micro-voids had no obvious changes when the strain was less than 20%, only the size distributions of micro-voids at some typical strain levels (i.e., 0%, 20%, 28%, 32% and 36%) were analyzed. It was observed that most micro-voids were small in size (20–40 μm) for the un-deformed specimen. Then some new small-sized (0–20 μm) micro-voids initiated and the inherent small-sized ones grew gradually as the tensile strain increased to 20%. With the further increase of strain, the number of middle-sized (40–100 μm) micro-voids increased significantly, and the total number of the micro-voids increased a lot. When the strain increased to 36%, the number of large-sized micro-voids (i.e., 100–180 μm) inside the specimen also increased significantly. In addition, there were no significant changes in several inherent large-sized micro-voids because they were away from the necking region.

The average size of micro-voids (ASMVs) and VFMVs of the RB specimen at different strain levels are shown in Fig. 7. It can be seen that the ASMVs experienced a slight decrease from 44.6 μm to 42.6 μm when the tensile strain increased from 0% to 12%; this was because the initiation of new micro-voids led to an increase in the total number, but at the same time the inherent micro-voids did not increase obviously in size. When the strain increased from 12% to 24%, the specimen undergone uniform and stable plastic deformation, i.e., the inherent micro-voids and the micro-voids initiated in the first stage (0–12%) grew slowly, while new micro-voids continue to be produced. The first two had a more significant influence on the micro-void size, so the ASMVs gradually increased. When the strain reached 28% and beyond, necking occurred and gradually aggravated. In this stage, the ASMVs increased rapidly to 73.9 μm with a linear trend until the strain reached 36%. Once the specimen fractured, the ASMVs deceased dramatically to 52.9 μm. This was because the large-sized micro-voids eventually evolved to macrocracks, and the specimen was then fractured from these macrocracks. Thus, the large-sized micro-voids disappeared and the ASMVs was reduced significantly. Different from the changes in ASMVs,

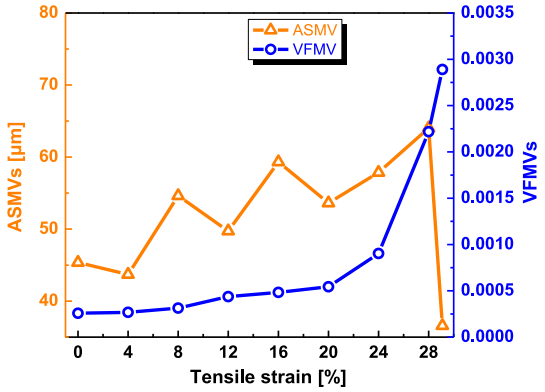

Fig. 10 – ASMVs and VFMVs of the NRB10 specimen during tensile deformation.

the VFMV kept increasing as the strain increased, and the increase in the VFMV followed a power function trend, i.e., it increased slowly when the strain was less than 24%, while increased rapidly from 0.0007 to 0.00317 with the increase of strain from 24% to 37.4%.

4.2.2. *Notched round bar (NRB) tensile specimens*

The micro-void evolutions of the middle parts of the NRB tensile specimens (NRB10 & NRB2) at different strain levels were also detected by X-ray CT, as visualized in Figs. 8 and 9. Unlike the micro-void evolution in the RB tensile specimen, i.e., no obvious changes in micro-voids until the tensile strain reached 20%, the micro-voids in the notched specimens began to evolve at lower strains. More specifically, the sizes of the inherent micro-voids began to increase and new small-sized micro-voids were initiated at strains of 16% and 8% for NRB10 and NRB2 specimens respectively. With a further increase in strain, the inherent micro-voids increased significantly and a large number were initiated, resulting in the occurrence of necking at the corresponding regions. Finally, the rapid increase in the number of new micro-voids and the significant growth in the inherent micro-voids led to the failure of NRB10 and NRB2 specimens at strains of 29.1% and 23.3% respectively.

The ASMVs and VFMVs at different strain levels for the NRB10 and NRB2 specimens are shown in Figs. 10 and 11

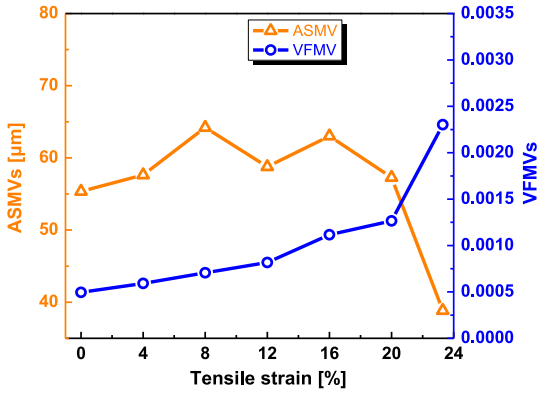

Fig. 11 – ASMVs and VFMVs of the NRB2 specimen during tensile deformation.

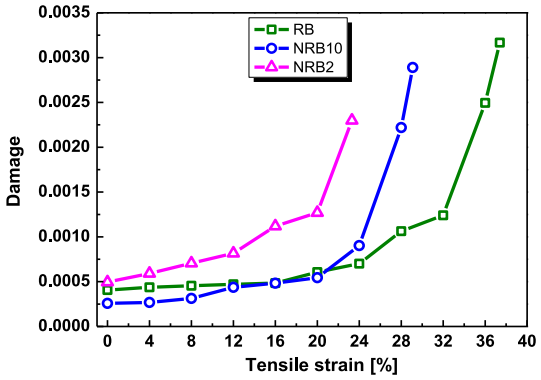

Fig. 12 – Damage evolution of the RB and NRB specimens during tensile deformation.

respectively. In contrast to the gradual increase in the ASMVs of the RB specimen after the strain exceeded 12%, the ASMVs fluctuated with increasing strain in the NRB specimens. When the growth of the inherent micro-voids was more pronounced than the initiation of new small-sized ones, the average sizes increased, and vice versa. On the other hand, the VFMV kept increasing with the increase of strain for both the NRB10 and NRB2 specimens. Since the key factor for the transformation of randomly formed micro-voids to eventual damage is the evolution of VFMV, the change of VFMV can be regarded as the damage evolution during the metal forming process, Fig. 12 shows the curves of damage evolutions for the RB and NRB specimens under tensile deformation. It can be seen that the notch sensitivity had a great influence on the damage evolution, i.e., the smaller the notch radius, the faster the damage evolution. In addition, the initial VFMVs of the tensile specimens (i.e., 0.0004068, 0.0002575 and 0.0004951 for RB, NRB10 and NRB2 respectively) were employed as the initial damage value f_0 for the subsequent damage prediction, and the experimental damage evolution data was further compared with the FE prediction results to verify the correctness of the simulation.

4.3. *Damage prediction and verification*

As described in Section 3, the proposed micro-damage model was compiled and implemented into ABAQUS using the subroutine UMAT for damage prediction. First, the comparison of the experimental load-elongation curves with the numerical predictions obtained from the FE simulations is shown in Fig. 13. It can be found that small standard error (SE) response is achieved for all the specimens, and a good agreement between the predictions and experiments is obtained. Then, the damage distribution and evolution of the tensile specimens were predicted and compared with the X-ray CT scanning results. The predicted damage distributions of the tensile specimens are shown in Fig. 14. In order to make the simulation and the experiment comparable, the strain corresponding to the predicted damage distribution was the same as the previous pause strain value at which the specimen fractured during the tensile test, that is: strain values of 36%, 28% and 20% were selected for RB, NRB10 and NRB2 specimens respectively. As can be seen from Fig. 14, RB tensile specimen had the most uniform plastic deformation, while the deformation of NRB specimens was mainly concentrated in the notch area. This was consistent with the deformation of the specimens measured from the tensile tests. Correspondingly, the damage was distributed throughout the gauge length of the RB specimen, however, the damage just occurred and concentrated in the notch of the NRB specimens. In addition, the most severe damage to all specimens was in the middle of the gauge length, and the smaller the notch radius, the more concentration the damage distribution, which was consistent with the result from experiment (enlarged view of FE prediction versus 2D section of X-ray CT scanning in the figure).

Although there was certain discrepancy in terms of damage distribution between the prediction and experiment (i.e.: the prediction shows more localized damage is distributed at the center and outer radii zones for the NRB10 and NRB2 specimens respectively, while that CT scanning demonstrates a more dispersed damage distribution at the necking regions for all specimens), the predicted damage was in good agreement with that of CT scanning (see Fig. 15, in which the predicted damage evolution curves were obtained by calculating the average damage value of each element at the neck region of the specimen). The experimental damage evolution data were also plotted as scattered points for comparison. It can be observed that the predicted damage evolution also followed the power function trend. By fitting the predicted curve in the form of $y = C + x^a$, the damage evolution rate a under different notch radius can be obtained, i.e., 6.212, 4.873 and 4.291 for RB, NRB10 and NRB2 specimen respectively. In addition, it can be

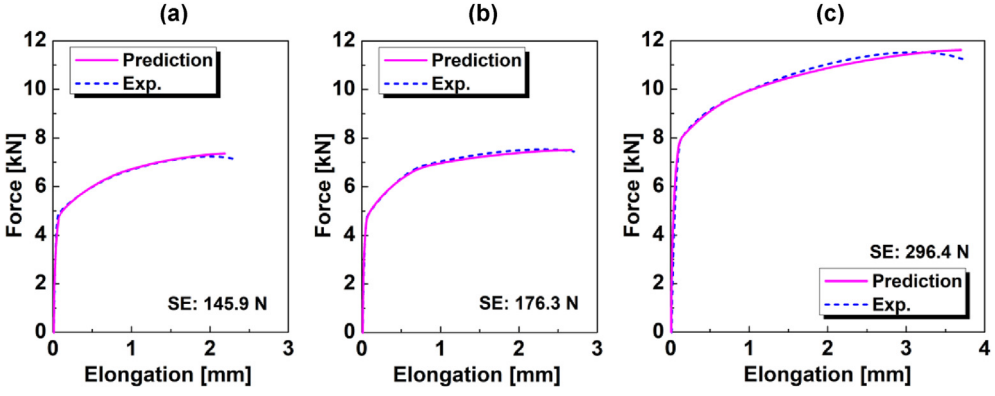

Fig. 13 – Comparison of load–elongation curves between FE predictions and uniaxial tensile tests: (a) NRB2; (b) NRB10; (c) RB.

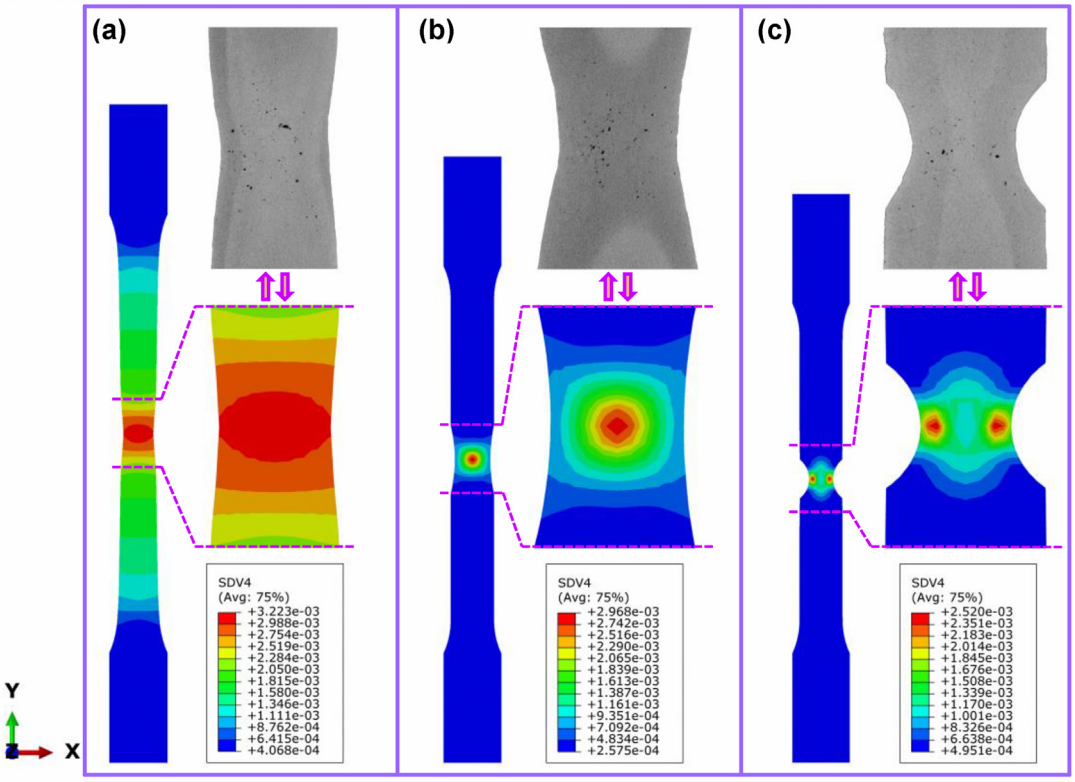

Fig. 14 – Predicted damage distribution and comparison with X-ray CT scanning for tensile specimens: (a) RB; (b) NRB10; (c) NRB2. (Note: all the simulated geometrical models were mirrored on the YZ plane for better demonstrating the internal damage distribution.)

found that the maximum damage value of the specimen decreased markedly with the decrease of notch radius. Since the maximum damage value indicates the allowable damage of the material, i.e., the greater the allowable damage, the stronger the ability of the material to resist fracture, it can be concluded that the RB specimen had better failure resistance then NRB specimen. Specifically, the allowable damage values for RB, NRB10 and NRB2 specimens under tension deformation were 0.00322, 0.00297 and 0.00252 respectively, and their corresponding fracture strains were 0.385, 0.289 and 0.230.

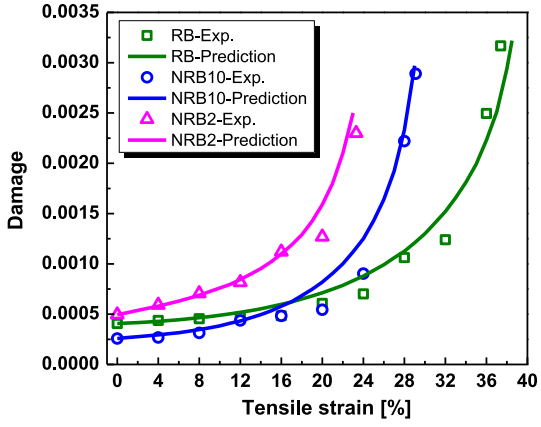

Fig. 15 – Comparison of damage evolution between FE prediction and X-ray CT scanning.

5. Conclusions

In this study, the nature of ductile damage, which involved the dynamic evolution mechanism of the nucleation, growth and coalescence of micro-voids, was revealed comprehensively by the combination of X-ray CT and loading-unloading tensile test. An improved micro-damage model was further developed for the damage prediction of tensile deformation. Following conclusions can be given.

(1) For the RB specimen, new small-sized micro-voids initiated and the inherent small-sized ones grew gradually as the tensile strain increased to 20%. Further increase of strain resulted in the number of middle-sized micro-voids increased significantly. In addition, the RB specimen experienced a uniform and stable plastic deformation stage when the strain increased from 12% to 24%. The dynamic changing in the newly formed and inherent micro-voids dominated the ASMV, i.e., ASMV experienced a slight decrease when the strain increased from 0% to 12%, then it increased gradually with the strain increased to 24%, afterward, it increased rapidly with a linear trend due to necking occurred, and finally it deceased dramatically because the large-sized micro-voids eventually evolved to macrocracks. Different from the changes in ASMV, the VFMV kept increasing as the

strain increased, and the increase in the VFMV followed a power function trend, i.e., it increased slowly when the strain was less than 24%, while it increased rapidly from 0.0007 to 0.00317 as the strain increased from 24% to 37.4%.

(2) For the NRB specimens, the micro-voids began to evolve at lower strains, i.e., the sizes of the inherent micro-voids began to increase and new small-sized micro-voids were initiated at strains of 16% and 8% for NRB10 and NRB2 specimens respectively. With a further increase in strain, the inherent micro-voids grew significantly and a large number of micro-voids were initiated, resulting in the occurrence of necking at the corresponding regions. In addition, the ASMVs fluctuated with increasing strain in the NRB specimens. When the growth of the inherent micro-voids was more pronounced than the initiation of new small-sized ones, the average sizes increased, and vice versa. On the other hand, the VFMV kept increasing with the increase of strain for both the NRB10 and NRB2 specimens. The notch sensitivity had a great influence on the damage evolution, i.e., the smaller the notch radius, the faster the damage evolution.

(3) Damage prediction for tensile deformation showed that the RB specimen had the most uniform plastic deformation, while the deformation of NRB specimens was mainly concentrated in the notch area. In addition, the most severe damage to all specimens was located in the middle of the gauge length, and the smaller the notch radius, the more concentration the damage distribution.

(4) The predicted damage evolution under tension followed the power function trend, which was in good agreement with the experiments. The maximum damage value of the specimen decreased markedly with the decrease of notch radius. Since the maximum damage value indicates the allowable damage of the material, i.e., the greater the allowable damage, the stronger the ability of the material to resist fracture, it can be concluded that the RB specimen had better failure resistance than the NRB specimen.

Declaration of Competing Interest

The authors declare that they have no known competing financial interests or personal relationships that could have appeared to influence the work reported in this paper.

Acknowledgments

The work described in this paper was partially supported by the grants from the Research Committee of The Hong Kong Polytechnic University under student account code RTBN, Research Institute for Advanced Manufacturing of The Hong Kong Polytechnic University, Hong Kong, Natural Science Foundation of Human Province, China (Nos. 2021JJ30719), Changsha Municipal Natural Science Foundation (No. 2014095) and State Key Laboratory of Metastable Materials Science and Technology, Yanshan University, China (No. 202107). The authors would like to acknowledge Dr. Y.L. Zhu for FE modelling assistance.

REFERENCES

[1] Tekkaya AE, Bouchard P-O, Bruschi S, Tasan CC. Damage in metal forming. CIRP Annals 2020;69(2):600–23.
[2] Zhao PJ, Chen ZH, Dong CF. Failure analysis based on microvoids damage model for DP600 steel on in-situ tensile tests. Eng Fract Mech 2016;154:152–68.
[3] Stock SR. Recent advances in X-ray microtomography applied to materials. Int Mater Rev 2008;53(3):129–81.
[4] Roth CC, Morgeneyer TF, Cheng Y, Helfen L, Mohr D. Ductile damage mechanism under shear-dominated loading: in-situ tomography experiments on dual phase steel and localization analysis. Int J Plast 2018;109:169–92.
[5] Croom BP, Burden D, Jin H, Vonk NH, Hoefnagels JPM, Smaniotto B, et al. Interlaboratory study of digital volume correlation error due to X-Ray computed tomography equipment and scan parameters: an update from the DVC challenge. Exp Mech 2021;61:395–410.
[6] Croom BP, Jin H, Carroll J, Long K, Li X. Particle clustering effects on damage mechanisms in elastomeric syntactic foams. Composites Part B 2019;175:107160.
[7] Luetje M, Wicke M, Bacaicoa I, Brueckner-Foit A, Geisert A, Fehlbier M. 3D characterization of fatigue damage mechanisms in a cast aluminum alloy using X-ray tomography. Int J Fatig 2017;103:363–70.
[8] Jia LJ, Zhang R, Zhou CF, Gu TY, Liu T, Xie JB, et al. In-situ three-dimensional X-ray investigation on micro ductile fracture mechanism of a high-Mn steel with delayed necking effect. J Mater Res Technol 2023;24:1076–87.
[9] Croom BP, Jin H, Noell PJ, Boyce BL, Li X. Collaborative ductile rupture mechanisms of high-purity copper identified by *in situ* X-ray computed tomography. Acta Mater 2019;181:377–84.
[10] Löffl Ch, Saage H, Göken M. In situ X-ray tomography investigation of the crack formation in an intermetallic beta-stabilized TiAl-alloy during a stepwise tensile loading. Int J Fatig 2019;124:138–48.
[11] Azghandi SHM, Weiss M, Arhatari BD, Adrien J, Maire E, Barnett MR. A rationale for the influence of grain size on failure of magnesium alloy AZ31: an in situ X-ray microtomography study. Acta Mater 2020;200:619–31.
[12] Croom BP, Xu P, Lahoda EJ, Deck CP, Li X. Quantifying the three-dimensional damage and stress redistribution mechanisms of braided SiC/SiC composites by *in situ* volumetric digital image correlation. Scripta Mater 2017;130:238–41.
[13] Wang ZY, Wu SC, Kang GZ, Li H, Wu ZK, Fu YN, et al. In-situ synchrotron X-ray tomography investigation of damage mechanism of an extruded magnesium alloy in uniaxial low-cycle fatigue with ratchetting. Acta Mater 2021;211:116881.
[14] Msolli S, Martiny M, Costa MC, Moreira LP, Mercier S, Molinari A. Numerical modeling of the deformation of AISI 304L using a tangent additive Mori-Tanaka homogenization scheme: application to sheet metal forming. J Mater Process Technol 2016;235:187–205.
[15] Wulfinghoff S, Fassin M, Reese S. A damage growth criterion for anisotropic damage models motivated from micromechanics. Int J Solid Struct 2017;121:21–32.
[16] Croom BP, Jin H, Mills B, Carroll J, Long K, Brown J, et al. Damage mechanisms in elastomeric foam composites: multiscale X-ray computed tomography and finite element analyses. Compos Sci Technol 2019;169:195–202.

[17] Lemaitre J. A continuous damage mechanics model for ductile fracture. J Eng Mater Technol 1985;107(1):83–9.
[18] Lemaitre J, Chaboche JL. Mechanics of solid materials. Cambridge: Cambridge University Press; 1990.
[19] Gurson AL. Continuum theory of ductile rupture by void nucleation and growth: Part I-Yield criteria and flow rules for porous ductile media. J Eng Mater Technol 1977;99(1):2–15.
[20] Needleman A, Tvergaard V. An analysis of ductile rupture in notched bars. J Mech Phys Solid 1984;32(6):461–90.
[21] Brünig M, Gerke S, Hagenbrock V. Micro-mechanical studies on the effect of the stress triaxiality and the Lode parameter on ductile damage. Int J Plast 2013;50:49–65.
[22] Guo YH, Xie YM, Wang DT, Du LF, Zhao JB. An improved damage-coupled viscoplastic model for predicting ductile fracture in aluminum alloy at high temperatures. J Mater Process Technol 2021;296:117229.
[23] Wu H, Xu WC, Shan DB, Jin BC. An extended GTN model for low stress triaxiality and application in spinning forming. J Mater Process Technol 2019;263:112–28.
[24] Aghaei M, Ziaei-Rad S. A micro mechanical study on DP600 steel under tensile loading using Lemaitre damage model coupled with combined hardening. Mater Sci Eng A 2020;772:138774.
[25] Yue ZM, Min XR, Tuo ZY, Soyarslan C, Zhuang XC, Badreddine H, et al. Broad stress triaxiality ratio band fracture experiments in DP900 metal sheets and corresponding predictive capability of advanced phenomenological and micromechanical fully coupled damage models. Mater Sci Eng A 2021;811:140978.
[26] Williams JJ, Flom Z, Amell AA, Chawla N, Xiao X, De Carlo F. Damage evolution in SiC particle reinforced Al alloy matrix composites by X-ray synchrotron tomography. Acta Mater 2010;58(18):6194–205.
[27] Cao T-S, Maire E, Verdu C, Bobadilla C, Lasne P, Montmitonnet P, et al. Characterization of ductile damage for a high carbon steel using 3D X-ray micro-tomography and mechanical tests—Application to the identification of a shear modified GTN model. Comput Mater Sci 2014;84:175–87.
[28] Kaye M, Puncreobutr C, Lee PD, Balint DS, Connolley T, Farrugia D, et al. A new parameter for modelling three-dimensional damage evolution validated by synchrotron tomography. Acta Mater 2013;61(20):7616–23.
[29] Lu XZ, Chan LC. Micro-voids quantification for damage prediction in warm forging of biocompatible alloys using 3D X-ray CT and RVE approach. J Mater Process Technol 2018;258:116–27.
[30] Suárez F, Sket F, Gálvez JC, Cendón DA, Atienza JM, Molina-Aldareguia J. The evolution of internal damage identified by means of X-ray computed tomography in two steels and the ensuing relation with Gurson's numerical modelling. Metals 2019;9(3):292.
[31] Xing L, Gao PF, Zhan M, Ren ZP, Fan XG. A micromechanics-based damage constitutive model considering microstructure for aluminum alloys. Int J Plast 2022;157:103390.
[32] Sancho A, Cox MJ, Cartwright T, Davies CM, Hooper PA, Dear JP. An experimental methodology to characterise post-necking behaviour and quantify ductile damage accumulation in isotropic materials. Int J Solid Struct 2019;176–177:191–206.
[33] Li H, Fu MW, Lu J, Yang H. Ductile fracture: experiments and computations. Int J Plast 2011;27(2):147–80.
[34] Lu XZ, Chan LC. Micromechanics-based damage model for failure prediction in cold forming. Mater Sci Eng A 2017;690:120–31.
[35] Santos RO, da Silveira LB, Moreira LP, Cardoso MC, da Silva FRF, dos Santos Paula A, et al. Damage identification parameters of dual-phase 600-800 steels based on experimental void analysis and finite element simulations. J Mater Res Technol 2019;8:644–59.
[36] Pardoen T, Hutchinson JW. An extended model for void growth and coalescence. J Mech Phys Solid 2000;48(12):2467–512.
[37] Bruhns OT, Xiao H, Meyers A. Self-consistent Eulerian rate type elasto-plasticity models based upon the logarithmic stress rate. Int J Plast 1999;15(5):479–520.
[38] Zhu YL, Kang GZ, Kan QH, Bruhn OT, Liu YJ. Thermo-mechanically coupled cyclic elasto-viscoplastic constitutive model of metals: theory and application. Int J Plast 2016;79:111–52.
[39] Zhu YL, Kang GZ, Kan QH, Bruhns OT. Logarithmic stress rate based constitutive model for cyclic loading in finite plasticity. Int J Plast 2014;54:34–55.
[40] Rousselier G. Dissipation in porous metal plasticity and ductile fracture. J Mech Phys Solid 2001;49(8):1727–46.
[41] Rousselier G. The Rousselier model for porous metal plasticity and ductile fracture. Handbook of Materials Behavior Models 2001;2:436–45.